

Doping-induced quantum spin Hall insulator to superconductor transition

Zhenjiu Wang,^{1,*} Yuhai Liu,^{2,3} Toshihiro Sato,¹ Martin Hohenadler,¹
Chong Wang,⁴ Wenan Guo,^{3,2} and Fakher F. Assaad^{1,5,†}

¹*Institut für Theoretische Physik und Astrophysik, Universität Würzburg, 97074 Würzburg, Germany*

²*Beijing Computational Science Research Center, 10 East Xibeiwang Road, Beijing 100193, China*

³*Department of Physics, Beijing Normal University, Beijing 100875, China*

⁴*Perimeter Institute for Theoretical Physics, Waterloo, Ontario, Canada N2L 2Y5*

⁵*Würzburg-Dresden Cluster of Excellence ct.qmat, Am Hubland, 97074 Würzburg, Germany*

A quantum spin Hall insulating state that arises from spontaneous symmetry breaking has remarkable properties: Skyrmion textures of the $SO(3)$ order parameter carry charge $2e$. Doping this state of matter opens a new route to superconductivity via the condensation of Skyrmions. We define a model amenable to large scale negative sign free quantum Monte Carlo simulations that allows us to study this transition. Our results support a direct and continuous doping induced transition between the quantum spin Hall insulator and s-wave superconductor. We can resolve dopings away from half-filling down to $\delta = 0.0017$. Such routes to superconductivity have been put forward in the realm of twisted bilayer graphene.

Introduction.— Doping a band insulator generically leads to a Fermi liquid state whose Fermi surface may become unstable to superconductivity. In contrast, insulating states where correlation effects are dominant provide different routes to superconductivity. Low lying Goldstone modes present in the insulating state can provide a glue between doped charge carriers. Spin fluctuation theories of high temperature superconductivity follow this idea [1, 2]. The correlated insulator can also contain preformed pairs that become charged upon doping. The resonating valence bond state based theory of high temperature superconductivity follows this idea [3, 4]. More recently, the idea of preformed pairs has been put forward in the realm of graphene Moiré superlattice systems [5] such as twisted bilayer graphene [6]. Here a correlation-induced topological insulator contains Skyrmions that carry charge $2e$ as low-lying excitations [7]. Upon doping superconductivity emerges due to the condensation of charged Skyrmions.

The model we will consider in this Letter differs significantly from the ones discussed in the realm of graphene Moiré superlattice systems but captures the essence of the aforementioned topological route to superconductivity. In Ref. 8, we introduced a model of Dirac fermions supplemented with a next-nearest-neighbor interaction term ($\sim \lambda$) and investigated its phase diagram at half-filling (see Fig. 1). The interaction dynamically generates a quantum spin Hall (QSH) insulating state that breaks $SU(2)$ spin rotational symmetry.

Upon further increasing λ at half-filling, the QSH state gives way to an s-wave superconductor (SSC). The QSH-SSC transition falls into the class of deconfined quantum critical points (DQCPs)[7]. Our previous work [8] suggests that both phase transitions are described by confor-

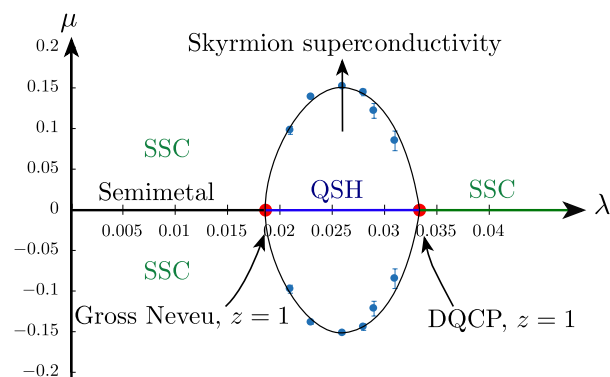


FIG. 1. Phase diagram of the model of Eq. 1 in the interaction strength, λ , versus chemical potential plane. The data at half-filling is reproduced from Ref. 8. The critical chemical potential μ_c at which the transition from the quantum spin Hall (QSH) to s-wave superconductor (SSC) occurs is computed by measuring the pairing gap at half-filling (see Ref. 9 and Fig. 3(a)).

mal field theories. The semimetal to QSH transition is in the Gross-Neveu-Yukawa universality class [10] whereas the DQCP is associated with a non-compact CP^1 [11] field theory describing the fractionalized $SO(3)$ order parameter.

The insulating QSH state has both preformed pairs, corresponding to Skyrmions of the QSH order parameter, and Goldstone modes. Understanding the fate of this state as a function of doping is the aim of this Letter. Our results are consistent with a doping-induced weakly first-order or continuous QSH-SSC transition driven by the condensation of Skyrmions.

Model and Method.—We consider a model of Dirac fermions in $2 + 1$ dimensions on the honeycomb lattice

* Zhenjiu.Wang@physik.uni-wuerzburg.de

† assaad@physik.uni-wuerzburg.de

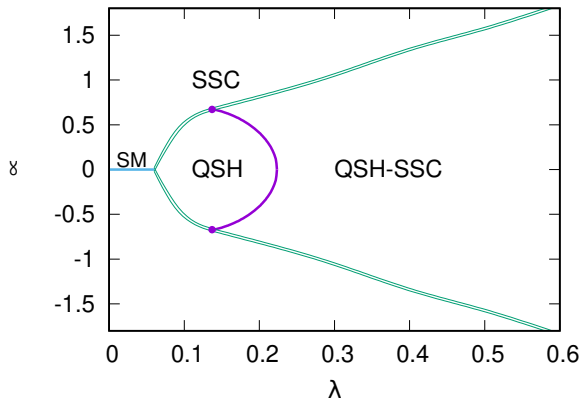


FIG. 2. Mean-field ground-state phase diagram. The blue and purple (green) lines correspond to continuous (first-order) transitions.

with Hamiltonian

$$\hat{H} = -t \sum_{\langle i,j \rangle} (\hat{c}_i^\dagger \hat{c}_j + H.c.) - \lambda \sum_{\square} \left(\sum_{\langle\langle ij \rangle\rangle \in \square} \hat{J}_{i,j} \right)^2 \quad (1)$$

with $\hat{J}_{i,j} = i\nu_{ij} \hat{c}_i^\dagger \boldsymbol{\sigma} \hat{c}_j + H.c.$ The spinor $\hat{c}_i^\dagger = (\hat{c}_{i,\uparrow}^\dagger, \hat{c}_{i,\downarrow}^\dagger)$ where $\hat{c}_{i,\sigma}^\dagger$ creates an electron at lattice site i with z -component of spin σ . The first term accounts for nearest-neighbor hopping. The second term is a plaquette interaction involving next-nearest-neighbor pairs of sites and phase factors $\nu_{ij} = \pm 1$ identical to the Kane-Mele model [12], see also Ref. [8]. Finally, $\boldsymbol{\sigma} = (\sigma^x, \sigma^y, \sigma^z)$ correspond to the Pauli spin matrices. We used the ALF (Algorithms for Lattice Fermions) implementation [13] of the well-established auxiliary-field quantum Monte Carlo (QMC) method [14–16]. Because $\lambda > 0$, we can use a real Hubbard-Stratonovich decomposition for the perfect square term. For each field configuration, time-reversal symmetry is present, even at finite chemical potential, so that eigenvalues of the fermion matrix occur in complex conjugate pairs. Hence, we do not suffer from the negative sign problem. In contrast to Ref. [8], we used a projective version of the algorithm (PQMC) [16–18]. The PQMC is a canonical approach in which the ground state is filtered out of a trial wave function that is chosen to be a Slater determinant. To avoid the negative sign problem, the trial wave function has to be time-reversal symmetric, so that we can only dope away from half-filling with Kramers pairs. For the considered trial wave function (see Ref. [9] for further details), we observed that a projection parameter set by the linear length of the lattice is sufficient to reach the ground state.

Mean-field approaches.—Before discussing our QMC results, it is instructive to carry out a mean-field approximation. When expanding the square in Eq. (1), diagonal terms, $\hat{J}_{i,j}^2$, contain, among other interactions, s-wave pair hopping terms that allow us to introduce an

SSC order parameter. The off-diagonal terms allow for QSH ordering (see Ref. [9] for a detailed calculation). As seen in Fig. 2, doping the semimetal produces the SSC. This reflects the pairing instability of Fermi surfaces to attractive interactions within Bardeen-Cooper-Schrieffer (BCS) theory. The protecting symmetries of the QSH state are related to time reversal and global charge conservation. Hence, the coexistence region (QSH+SSC) is topologically trivial. Furthermore, the transition at half-filling from the QSH to QSH+SSC is continuous and does not require the closing of the single-particle gap. Upon doping, the mean-field approximation generically supports two scenarios: (i) a continuous transition with dynamical exponent $z = 2$ from the QSH to QSH+SSC, (ii) a first-order transition from the QSH to SSC [19]. Our mean-field approximation provides examples of both scenarios. As expected, it fails to capture the DQCP between the QSH and SSC phases at half-filling [8].

QMC results.—We now turn to unbiased QMC results which, in contrast to the mean-field approach, capture Goldstone modes as well as topological Skyrmion excitations. We consider $t = 1$ and $\lambda = 0.026$, which places us in the center of the QSH phase at half-filling.

At this filling, we show in Fig. 3 the momentum dependence of the spin-orbit coupling gap $\Delta_{\text{QSH}}(\mathbf{q})$ and the SSC gap $\Delta_\eta(\mathbf{q})$. To obtain these data, we measured the imaginary-time displaced correlation functions of the spin-orbit coupling operators $\hat{\mathcal{O}}_{\mathbf{r},n}^{\text{QSH}} = \hat{J}_{\mathbf{r}+\boldsymbol{\delta}_n, \mathbf{r}+\boldsymbol{\eta}_n}$. Here, \mathbf{r} denotes a unit cell and n runs over the six next-nearest neighbor bonds of the corresponding hexagon with legs $\mathbf{r} + \boldsymbol{\delta}_n$ and $\mathbf{r} + \boldsymbol{\eta}_n$. We also consider the s-wave pairing operators $\hat{\eta}_{\mathbf{r},\tilde{\delta}}^+ = \hat{c}_{\mathbf{r}+\tilde{\delta},\uparrow}^\dagger \hat{c}_{\mathbf{r}+\tilde{\delta},\downarrow}^\dagger$, where $\tilde{\delta}$ runs over the two orbitals in unit cell \mathbf{r} . The gaps were obtained from

$$\begin{aligned} S^{\text{QSH}}(\mathbf{q}, \tau) &= \sum_n \langle \hat{\mathcal{O}}_{\mathbf{q},n}^{\text{QSH}}(\tau) \hat{\mathcal{O}}_{-\mathbf{q},n}^{\text{QSH}}(0) \rangle \propto e^{-\Delta_{\text{QSH}}(\mathbf{q})\tau} \\ S^{\text{SSC}}(\mathbf{q}, \tau) &= \sum_{\tilde{\delta}} \langle \hat{\eta}_{\mathbf{q},\tilde{\delta}}^+(\tau) \hat{\eta}_{\mathbf{q},\tilde{\delta}}^-(0) + \hat{\eta}_{\mathbf{q},\tilde{\delta}}^-(\tau) \hat{\eta}_{\mathbf{q},\tilde{\delta}}^+(0) \rangle \\ &\propto e^{-\Delta_\eta(\mathbf{q})\tau}, \end{aligned} \quad (2)$$

in the limit of large imaginary time τ [9]. As expected for a Goldstone mode, $\Delta_{\text{QSH}}(\mathbf{q})$ in Fig. 3(b) exhibits a gapless, linear dispersion around the ordering wave vector $\mathbf{q} = \Gamma$. On the other hand, $\Delta_\eta(\mathbf{q})$ remains clearly nonzero with quadratic dispersion (see Fig. 3(a)). It is also important to note that an s-wave pair has a smaller excitation energy than twice the single-particle gap, as shown in the inset of Fig. 3(a). Thus, pairing is present and we can foresee that these preformed pairs will condense to form a superconducting state upon doping.

A key quantity to understand the nature of the metal or superconductor to insulator transition is the behavior of the chemical potential upon doping away from half-filling [20–22]. For first-order transitions, μ shows a jump. For continuous transitions, and with the assumption of a single length scale, the singular part of the free

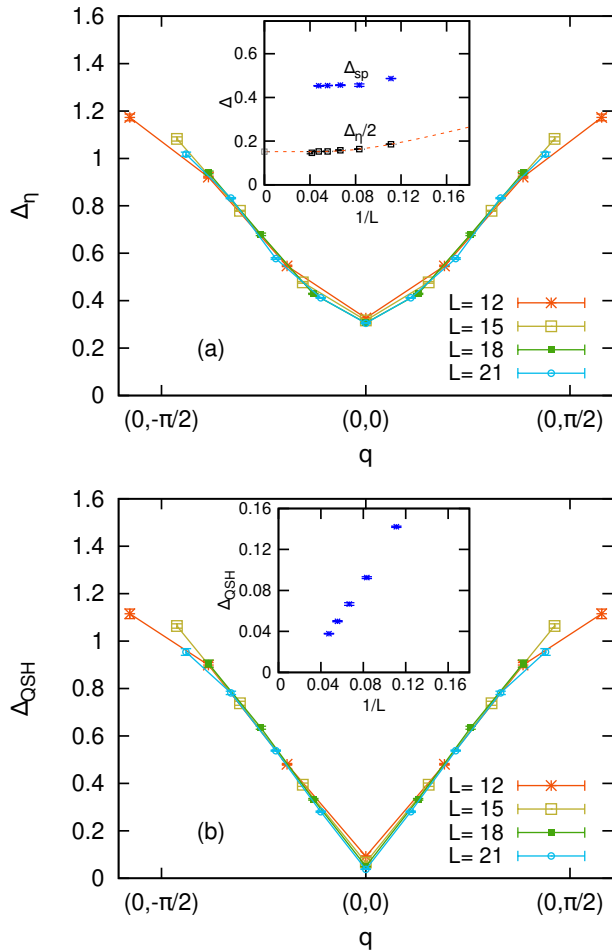


FIG. 3. Momentum dependence of (a) the pairing gap and (b) the QSH gap for the half-filled case, in the vicinity of Γ point along the direction towards the M point in the Brillouin zone of the honeycomb lattice. The inset of (a) shows the $1/L$ dependence of the single-particle gap Δ_{sp} and half of the s -wave pairing gap $\Delta_{\eta}/2$. The inset of (b) shows the QSH gap, Δ_{QSH} , versus $1/L$.

energy scales as $f \propto |\mu - \mu_c|^{\nu(d+z)}$ with d the dimensionality and ν (z) the correlation length (dynamical) exponent. Since the doping defined as $1 - n$ is proportional to $\partial f / \partial \mu$ and the compressibility is associated with twisting boundaries in the imaginary-time direction, one can show that for transitions driven via the chemical potential the hyper scaling relation $\nu z = 1$ holds. Thereby, $\delta \propto |\mu - \mu_c|^{\nu d}$. Doping a band insulator satisfies the hyper-scaling assumption. For a quadratic band, $z = 2$ so that $\delta \propto |\mu - \mu_c|^{d/2}$. This scaling behavior is satisfied upon doping a bosonic Mott insulator [22].

With the PQMC, we can compute the ground-state energy for a given, even particle number N_p and then derive the chemical potential. However, we found it more efficient to extract μ from an estimate of $\Delta_{\eta^-}(N_p)$ by analyzing the long imaginary time behavior of the pair correlation

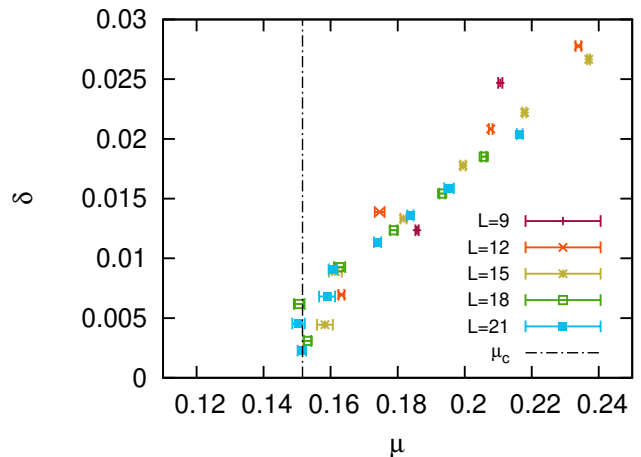


FIG. 4. Doping factor δ as a function of chemical potential $\mu \equiv \frac{\Delta_{\eta^-}}{2}$ for sizes $L = 9, 12, 15, 18,$ and 21 . The red dashed line is the critical chemical potential from the extrapolated pairing gap $\Delta_{\eta}/2$ shown in Fig. 3.

relation function $\sum_{\delta} \langle \hat{\eta}_{\mathbf{q},\delta}^+(\tau) \hat{\eta}_{\mathbf{q},\delta}^-(0) \rangle \sim e^{-\Delta_{\eta^-} \tau}$, where $\mathbf{q} = \Gamma$. In particular,

$$\mu \equiv \frac{E(N_p) - E(N_p - 2)}{2} = \frac{\Delta_{\eta^-}(N_p)}{2}. \quad (3)$$

With the doping relative to half-filling defined as $\delta \equiv 1 - \frac{N_p - 1}{2L^2}$ [23], we obtain the data shown in Fig. 4. For alternative ways of computing μ see the SM [9].

Figure 4 plots δ as a function of μ . The vertical dash-dotted line corresponds to the critical chemical potential. The data support a linear behavior for $\mu > 0.16$, but this form would overshoot the critical chemical potential. In a narrow window of dopings, $\delta < 0.01$, we observe a downturn in the functional form. Within our precision, we can offer two interpretations: a weakly first-order transition or a continuous transition with dynamical exponent $z > 2$. We note that continuous metal-insulator transitions with $z > 2$ have been put forward in the context of doped quantum antiferromagnets [20, 24].

Another important question to answer is if the onset of superconductivity is tied to the vanishing of the QSH order parameter. To this end, we consider the renormalization-group invariant correlation ratios ($\alpha = \text{QSH, SSC}$)

$$R_{\alpha} \equiv 1 - \frac{S^{\alpha}(\mathbf{q}_0 + \delta \mathbf{q})}{S^{\alpha}(\mathbf{q}_0)} \quad (4)$$

based on the equal-time correlation functions of the spin current and s -wave pairing operators in momentum space, $S^{\alpha}(\mathbf{q})$. Here, $\mathbf{q}_0 = (0, 0)$ is the ordering wave vector and $\mathbf{q}_0 + \delta \mathbf{q}$ a neighboring wave vector. By definition, $R_{\alpha} \rightarrow 1$ ($\rightarrow 0$) in the ordered (disordered) state for $L \rightarrow \infty$. At a critical point, R_{α} is scale invariant and for sufficiently

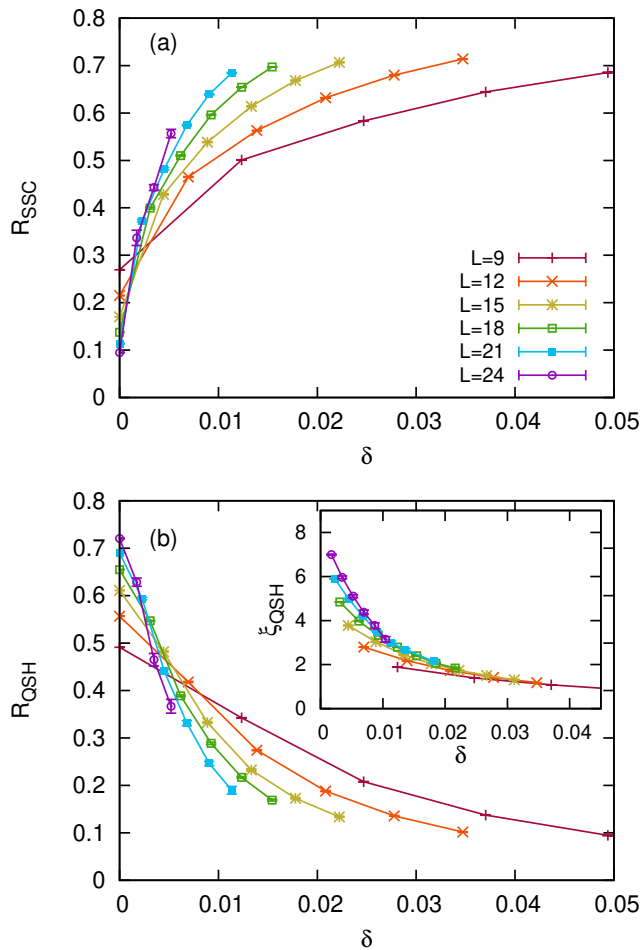


FIG. 5. Correlation ratios for (a) SSC and (b) QSH orders as a function of doping δ . The system sizes are $L = 9, 12, 15, 18, 21,$ and 24 . The inset of (b) shows the δ -dependence of the finite-size correlation length for the QSH order parameter.

large L , one should observe a crossing in R_α for different system sizes. Figures 5(a) and (b) show results for R_{SSC} and R_{QSH} as a function of δ . Due to the observed binding of electrons in the insulating state, we expect superconductivity for any $\delta > 0$. This is confirmed by Fig. 5(a). The drift in the crossings due to corrections to scaling is consistent with $\delta_c^{\text{SSC}} \rightarrow 0$ in the thermodynamic limit. The same quantity is plotted for the QSH correlation ratio in Fig. 5(b). The data show that the QSH order parameter vanishes very rapidly as a function of doping. Again, the drift of the crossing point as a function of system size scales to smaller values of δ . Given the data, we can provide an upper bound $\delta_c^{\text{QSH}} < 0.0017$ which corresponds to our resolution [25]. In our interpretation of Fig. 4, we could not exclude the possibility of a weakly first-order transition. On our finite systems, neither of the correlation ratios show a discontinuity, consistent with a continuous transition.

As a crosscheck, we consider the second-moment,

finite-size correlation length [26], $\xi_\alpha^2 \equiv \frac{\sum_{\mathbf{r}} |\mathbf{r}|^2 S^\alpha(\mathbf{r})}{\sum_{\mathbf{r}} S^\alpha(\mathbf{r})}$, obtained from the real-space, equal-time correlation functions [27]. The inset of Fig. 5(b) reveals the absence of saturation of the QSH correlation length at any finite doping $\delta > 0.0017$. Saturation would be expected for a first-order transition.

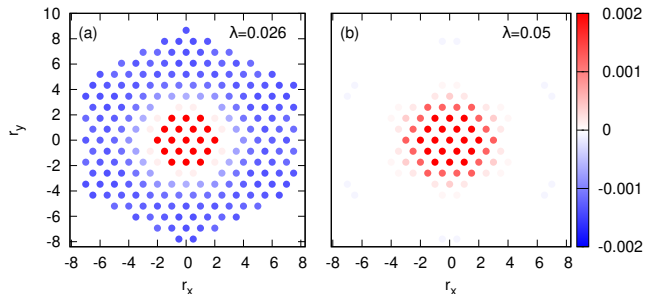


FIG. 6. Real space equal time correlation function of the QSH order parameter around a pinned hole pair at the origin. To the Hamiltonian of Eq. 1 we include the pinning potential: $\hat{H}_{\text{pin}} \equiv C \sum_{\mathbf{r}} \sum_{\delta} e^{-|\mathbf{r}+\delta|/\xi} \hat{c}_{\mathbf{r}+\delta}^\dagger \hat{c}_{\mathbf{r}+\delta}$ with $C = 1$ and $\xi = 1$. We consider $L = 15$, at (a) $\lambda = 0.026$ and (b) $\lambda = 0.05$.

The notion of Skyrmion superconductivity hinges on a locking in of the charge density and texture of the $\text{SO}(3)$ QSH order parameter. To image this, we dope two holes away from half-filling and localize them by modulating the chemical potential. The real space correlations of the QSH order parameter are then expected to show a texture akin to a Skyrmion. Precisely this is seen in Fig. 6(a) at $\lambda = 0.026$. In contrast *far* away from the QSH state at $\lambda = 0.05$ (see Fig. 6(b)) a Skyrmion is not present around the localized pair.

Discussion and summary.—Our data suggest a doping-induced, continuous and direct phase transition between the QSH state and the SSC. Clearly, we cannot exclude the possibility of a weakly first-order transition in which the correlation length saturates beyond our maximum system size ($L = 24$). Our dynamically generated QSH state possesses Goldstone modes and charge- $2e$ Skyrmions of the QSH order parameter. The Goldstone modes correspond to long-wavelength fluctuations of the spin-orbit coupling and do not break time-reversal symmetry. Hence, single-particle spin-flip scattering off Goldstone modes—as present in doped quantum antiferromagnets—is not allowed. Remarkably, one can also show that $[\hat{c}_{\mathbf{k}=0}, \hat{H}_\lambda] = 0$ (see Ref. [9]), so that at the Γ point the single-particle spectral function [9] is unaffected by the interaction \hat{H}_λ . This is in strong contrast to quantum antiferromagnets, where Goldstone modes couple to single-particle excitations to form a narrow band of spin polarons [28–30]. These arguments suggest that Goldstone modes do not provide the glue that leads to pairing.

We interpret our results in terms of preformed pairs,

Skyrmions carrying charge $2e$, that condense upon doping. In fact, by pinning the charge we were able to image the Skyrmion. Within this picture, the correlation length that diverges at the transition corresponds to the average distance between Skyrmions.

The finite-temperature phase diagram remains to be analyzed. Such calculations could reveal pseudo-gap physics related to preformed pairs at small doping. At large dopings, a crossover to conventional superconductivity is expected.

FFA acknowledges many insightful discussions with M. Imada on the topic of metal-insulator transitions. ZW would like to thank M. Ulybyshev and X. Wu for useful discussions on twisted bilayer graphene. The authors gratefully acknowledge the Gauss Centre for Supercomputing e.V. (www.gauss-centre.eu) for funding this project by providing computing time on the GCS Supercomputer SUPERMUC-NG at Leibniz Supercomputing Centre (www.lrz.de). FFA thanks funding from the Deutsche Forschungsgemeinschaft under the grant number AS 120/15-1 as well as the Würzburg-Dresden Cluster of Excellence on Complexity and Topology in Quantum Matter ct.qmat (EXC 2147, project-id 390858490). ZW thanks financial support from the DFG funded SFB 1170 on Topological and Correlated Electronics at Surfaces and Interfaces. TS thanks funding from the Deutsche Forschungsgemeinschaft under the grant number SA 3986/1-1. Y.L. was supported by the China Postdoctoral Science Foundation under Grants No.2019M660432 as well as the National Natural Science Foundation of China under Grants No.11947232 and No.U1930402. Research at Perimeter Institute (C.W.) is supported by the Government of Canada through the Department of Innovation, Science and Economic Development Canada and by the Province of Ontario through the Ministry of Research, Innovation and Science. W.G. was supported by the National Natural Science Foundation of China under Grants No. 11775021 and No. 11734002.

[1] R. Coldea, S. M. Hayden, G. Aeppli, T. G. Perring, C. D. Frost, T. E. Mason, S.-W. Cheong, and Z. Fisk, *Phys. Rev. Lett.* **86**, 5377 (2001).
 [2] D. J. Scalapino, *Rev. Mod. Phys.* **84**, 1383 (2012).
 [3] P. W. Anderson, *Science* **235**, 1196 (1987).
 [4] P. Lee, N. Nagaosa, and X. Wen, *Rev. Mod. Phys.* **78**, 17 (2006).
 [5] Y.-H. Zhang, D. Mao, Y. Cao, P. Jarillo-Herrero, and T. Senthil, *Phys. Rev. B* **99**, 075127 (2019).
 [6] E. Khalaf, S. Chatterjee, N. Bultinck, M. P. Zaletel, and A. Vishwanath, [arXiv:arXiv2004.00638](https://arxiv.org/abs/2004.00638).
 [7] T. Grover and T. Senthil, *Phys. Rev. Lett.* **100**, 156804 (2008).
 [8] Y. Liu, Z. Wang, T. Sato, M. Hohenadler, C. Wang, W. Guo, and F. F. Assaad, *Nature Commun.* **10**, 2658 (2019).

[9] See Supplemental Material.
 [10] D. J. Gross and A. Neveu, *Phys. Rev. D* **10**, 3235 (1974).
 [11] T. Senthil, A. Vishwanath, L. Balents, S. Sachdev, and M. P. Fisher, *Science* **303**, 1490 (2004).
 [12] C. L. Kane and E. J. Mele, *Phys. Rev. Lett.* **95**, 146802 (2005).
 [13] M. Berx, F. Goth, J. S. Hofmann, and F. F. Assaad, *SciPost Phys.* **3**, 013 (2017).
 [14] R. Blankenbecler, D. J. Scalapino, and R. L. Sugar, *Phys. Rev. D* **24**, 2278 (1981).
 [15] S. R. White, D. J. Scalapino, R. L. Sugar, E. Y. Loh, J. E. Gubernatis, and R. T. Scalettar, *Phys. Rev. B* **40**, 506 (1989).
 [16] F. Assaad and H. Evertz, in *Computational Many-Particle Physics*, Lecture Notes in Physics, Vol. 739, edited by H. Fehske, R. Schneider, and A. Weiße (Springer, Berlin Heidelberg, 2008) pp. 277–356.
 [17] G. Sugiyama and S. Koonin, *Annals of Physics* **168**, 1 (1986).
 [18] S. Sorella, S. Baroni, R. Car, and M. Parrinello, *Europhys. Lett.* **8**, 663 (1989).
 [19] An intermediate metallic state would be unstable to pairing and we have excluded fine-tuning.
 [20] M. Imada, A. Fujimori, and Y. Tokura, *Rev. Mod. Phys.* **70**, 1039 (1998).
 [21] F. F. Assaad and M. Imada, *Phys. Rev. B* **58**, 1845 (1998).
 [22] M. P. A. Fisher, P. Weichman, G. Grinstein, and D. S. Fisher, *Phys. Rev. B* **40**, 546 (1989).
 [23] Here, $N_p - 1$ is the thermal average of particle numbers, with the N_p and the $N_p - 2$ sector tuned to have the same ground-state energy at the chemical potential defined in Eq. (3).
 [24] F. F. Assaad and M. Imada, *Phys. Rev. Lett* **76**, 3176 (1996).
 [25] Since we are working in the canonical ensemble, the smallest doping is set by $2/(2L^2)$.
 [26] F. Parisen Toldin, M. Hohenadler, F. F. Assaad, and I. F. Herbut, *Phys. Rev. B* **91**, 165108 (2015).
 [27] The fact that there is no additional phase factor in the above summations comes from the known ordering wave vector $\mathbf{k} = \Gamma$.
 [28] G. Martinez and P. Horsch, *Phys. Rev. B* **44**, 317 (1991).
 [29] R. Preuss, W. Hanke, and W. von der Linden, *Phys. Rev. Lett.* **75**, 1344 (1995).
 [30] M. Raczkowski, R. Peters, T. T. Phung, N. Takemori, F. F. Assaad, A. Honecker, and J. Vahedi, *Phys. Rev. B* **101**, 125103 (2020).
 [31] F. F. Assaad and M. Imada, *J. Phys. Soc. Jpn.* **65**, 189 (1996).

SUPPLEMENTAL MATERIAL

Projective QMC approach

We used the projective QMC algorithm of the ALF-library [13]. This canonical algorithm filters out the ground state, $|\psi_0\rangle$, from a trial wave function, $|\psi_T\rangle$, that is required to be non-orthogonal to the ground state:

$$\frac{\langle\psi_0|\hat{O}|\psi_0\rangle}{\langle\psi_0|\psi_0\rangle} = \lim_{\Theta\rightarrow\infty} \frac{\langle\psi_T|e^{-\Theta\hat{H}}\hat{O}e^{-\Theta\hat{H}}|\psi_T\rangle}{\langle\psi_T|e^{-2\Theta\hat{H}}|\psi_T\rangle}. \quad (5)$$

The trial wave function $|\psi_T\rangle$ is chosen to be a Slater determinant with N_p particles ($\hat{N}|\psi_T\rangle = N_p|\psi_T\rangle$). In particular,

$$|\psi_T\rangle = |\psi_T^\uparrow\rangle \otimes |\psi_T^\downarrow\rangle \quad (6)$$

with

$$|\psi_T^\sigma\rangle \equiv \prod_{n=1}^{N_p/2} \left(\sum_{\mathbf{i}} \hat{c}_{\mathbf{i},\sigma}^\dagger U_{\mathbf{i},n} \right) |0\rangle. \quad (7)$$

$U_{\mathbf{i},n}$ is the n^{th} single-particle eigenstate, ordered in ascending energy eigenvalues, of the spinless fermion Hamiltonian

$$\hat{H} = -t \sum_{\langle\mathbf{i},\mathbf{j}\rangle} (\hat{c}_{\mathbf{i}}^\dagger \hat{c}_{\mathbf{j}} + H.c.) + \sum_{\langle\mathbf{i},\mathbf{j}\rangle} \xi_{\mathbf{i},\mathbf{j}} (\hat{c}_{\mathbf{i}}^\dagger \hat{c}_{\mathbf{j}} + H.c.). \quad (8)$$

The first term corresponds to the tight-binding Hamiltonian on the honeycomb lattice. We require the perturbing hopping matrix elements $|\xi_{\mathbf{i},\mathbf{j}}| \ll t$ and $\text{Im} \xi_{\mathbf{i},\mathbf{j}} = 0$. The sign and modulus of $\xi_{\mathbf{i},\mathbf{j}}$ are chosen randomly so that all energy eigenvalues of the spinless Hamiltonian are non-degenerate. Our trial wave function hence breaks lattice and point group symmetries. Crucially, however, time-reversal symmetry is present. Since $\lambda > 0$ (see Eq. (1)), we can decouple the interaction with a real Hubbard-Stratonovich transformation such that both the imaginary time propagation and the trial wave function are invariant under time reversal:

$$T\alpha \begin{pmatrix} \hat{c}_{\mathbf{i},\uparrow} \\ \hat{c}_{\mathbf{i},\downarrow} \end{pmatrix} T^{-1} = \bar{\alpha} \begin{pmatrix} \hat{c}_{\mathbf{i},\downarrow} \\ -\hat{c}_{\mathbf{i},\uparrow} \end{pmatrix}. \quad (9)$$

Hence, the eigenvalues of the fermion matrix come in complex conjugate pairs and no negative sign problem occurs.

A projection length $\Theta = L$ was found to be sufficient to converge to the finite-size ground state for all of our system sizes. We have used an imaginary time step $\Delta\tau = 0.2$ and a symmetric Trotter decomposition to guarantee the Hermiticity of the imaginary time propagator. All calculations were carried out at $\lambda = 0.026$ in units where $t = 1$.

Equal-time structure factor

In Fig. 7, we show the momentum dependence of the equal-time QSH and SSC structure factors at $\delta = 0$ and at $\delta = 1/36$. Upon doping, the QSH structure factor does not develop incommensurate features. At $\delta = 1/36$, the QSH data (Fig. 7(b)) are consistent with the absence of long-range order, whereas the SSC structure factor (Fig. 7(d)) shows a marked increase as a function of system size.

The onset of long-range order as well as a measure for the correlation length can be obtained by considering $1/S(\mathbf{Q} = 0)$ as function of δ (see Fig. 8). The SSC ordering appears immediately at $\delta > 0$, characterized by the quick decay of $1/S_{\text{SSC}}$ as function of system size. In particular, $1/S_{\text{SSC}}$ shows no saturation as a function of system size. On the other hand, $1/S_{\text{QSH}}$ shows a clear saturation at *large* doping. For a given doping, the lattice size at which this quantity converges is a measure of the correlation length. Upon inspection, one will see that larger lattice sizes are required to achieve convergence upon approaching half-filling. In particular, following the envelope of these curves again suggests that the correlation length of the QSH fluctuations grows continuously and diverges as $\delta \rightarrow 0$. This is consistent with the data shown in the main text.

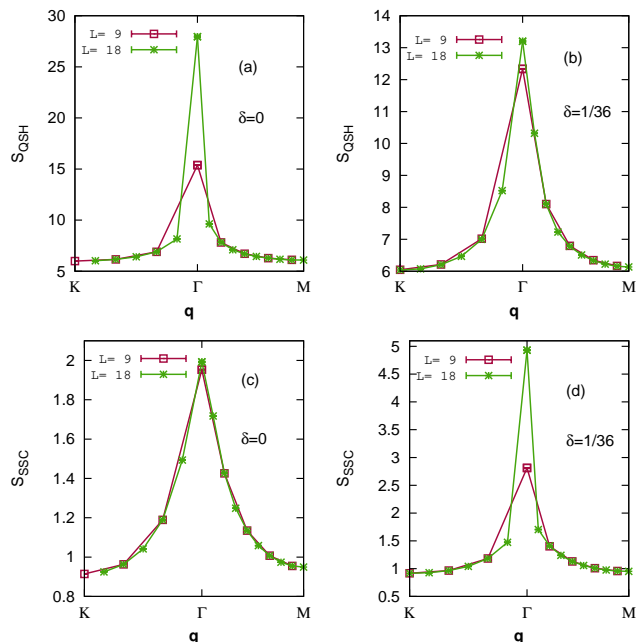


FIG. 7. Momentum dependence of the equal-time structure factor for ((a),(b)) QSH and ((c),(d)) SSC operators for ((a),(c)) $\delta = 0$ and and ((b),(d)) $\delta = \frac{1}{36}$.

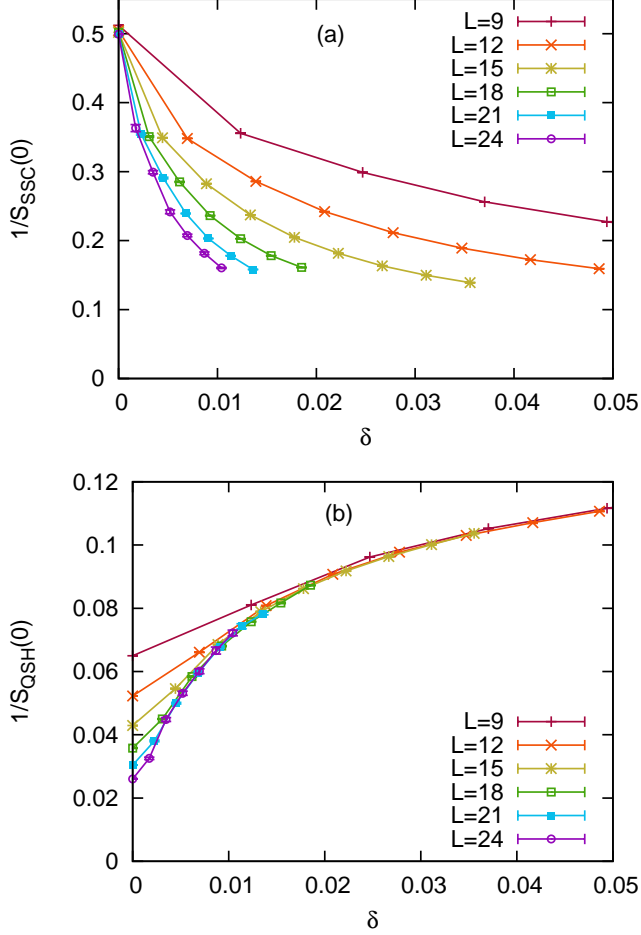


FIG. 8. δ dependence of $1/S(\mathbf{Q} = 0)$ for SSC (a) and QSH (b), as a function of δ , for $L = 9, 12, 15, 18, 21$ and 24

Consistency check of the pairing gap

We check the consistency of our evaluation of the ground-state energy difference between different even particle-number sectors:

$$E(N_p) - E(N_p - 2) = \Delta_{\eta^-}(N_p) = \Delta_{\eta^+}(N_p - 2) \quad (10)$$

where $E(N_p)$ is the ground state energy measured within the PQMC in the N_p particle number sector; $\Delta_{\eta^-}(N_p)$ is the s-wave pairing (η^-) gap extrapolated from the time-displaced correlation function.

The imaginary-time domain β , in which we measure the time-displaced correlation function, is set to $\beta = L$ for $L = 9, 12, 15$, and 18 , and to $\beta = 10$ for $L = 21$. To extrapolate the pairing gap, we use sequential fits

$$\langle \eta^+(m\tau_0 + \tau)\eta^-(m\tau_0) \rangle \propto e^{-\Delta_m \tau} \quad m = 0, 1, 2, 3... \quad (11)$$

where $\tau_0 = 1.0$ and $\tau \in [0, \tau_0)$. The gap is extrapolated as

$$\Delta_m - \Delta(m \rightarrow \infty) \propto e^{-am} \quad (12)$$

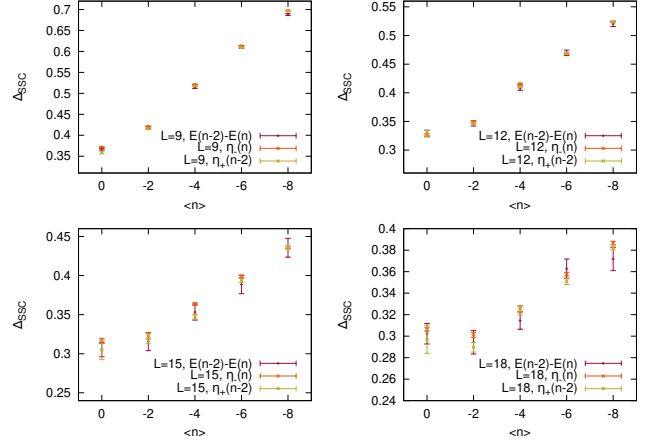


FIG. 9. Three ways of pairing gap evaluation for (a) $L = 9$, (b) 12 , (c) 15 , and (d) 18 , for doped particle number $N_p - 2L^2 = 0, -2, -4, -6$ and -8 .

where a is optimized for the best fit.

In Fig. 9, we show that the three different ways of evaluating the gap give consistent results for $L = 9, 12, 15$, and 18 for several particle-number sectors near half-filling. In particular, one can compute the ground-state energy and take the difference or measure time-displaced correlation functions of the pair adding or removal operator. Using the energy difference generically produces bigger error bars. Here, we carry out two independent simulations and thereby have to add the errors on two extensive quantities (total energies) to estimate the error on an intensive one, the total energy difference. Hence to keep the error bar on the total energy difference, we have to scale the error on the energy per site as $1/L^2$. Even taking into account self-averaging on large system sizes, this proves to be numerically expensive.

Gap extrapolation at half filling

In this section we discuss the calculations carried out to determine the phase boundary of Fig. 1. As explained in the main text, the critical chemical potential is obtained from half the pairing gap Δ_η at half filled case.

Fig. 10 shows the extrapolation of the pairing gap Δ_η at $\mu = 0$, for four different values of λ inside the QSH phase. An exponential finite size behavior is assumed for the extrapolation:

$$\Delta_\eta(L) = \Delta_\eta(L \rightarrow \infty) + ae^{-L/\xi} \quad (13)$$

For $\lambda = 0.021, 0.023$ and 0.028 , an acceptable χ^2 is obtained for a collective fit using sizes $L = 6, 9, \dots, 21$. For $\lambda = 0.031$, an acceptable χ^2 is obtained when the $L = 6$ data is omitted.

Additionally we show the single particle gap at $\mu = 0$ as extracted from the imaginary time displaced Green

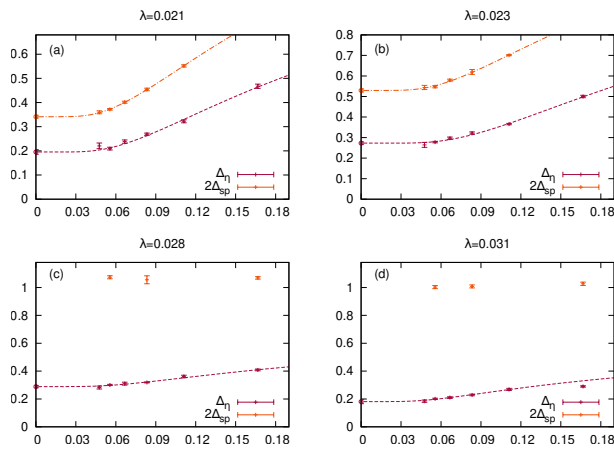


FIG. 10. Pairing and single particle gap extrapolation at half-filling, for $\lambda = 0.021, 0.023, 0.028$ and 0.031 .

function:

$$\langle c_{\mathbf{k}}(\tau)c_{\mathbf{k},\alpha}^{\dagger}(0) \rangle \propto e^{-\Delta_{\text{sp}}\tau}. \quad (14)$$

Due to the shift of the minimal gap in momentum space at large λ , we choose $\mathbf{k} \equiv (\frac{4\pi}{3}, 0)$ for $\lambda = 0.021, 0.023$ and 0.026 , and $\mathbf{k} \equiv (\pi, \frac{\pi}{\sqrt{3}})$ for $\lambda = 0.028$ and 0.031 .

To extrapolate to the thermodynamic limit, we have again used an exponential fit,

$$\Delta_{\text{sp}}(L) = \Delta_{\text{sp}}(L \rightarrow \infty) + ae^{-L/\xi}, \quad (15)$$

that is supported by the data.

Before proceeding, we would like to comment on the exponential fit, since it is unexpected. In principle, a doped hole (or pair) will couple to the Goldstone modes such that one expects the finite size effects of the gap to pick up the finite size behavior of the Goldstone mode. The latter follow a polynomial law in $1/L$. This behavior is explicitly seen in the context of antiferromagnetic Mott insulators [31]. If on the other hand the doped charge carriers do not couple strongly to the low-lying Goldstone modes, then we expect dominant exponential finite size effects. This point of view will be confirmed in the next section.

Single-particle spectrum at finite doping

We consider the single-particle spectral function at finite doping. Away from half-filling, particle-hole symmetry is broken and we have to separately calculate the spectra for electron addition and removal,

$$A(\mathbf{k}, \omega) = \frac{1}{Z} \sum_n (|\langle n|c_{\mathbf{k}}|0 \rangle|^2 \delta(E_n - E_0 - \omega)) + \frac{1}{Z} \sum_m (|\langle m|c_{\mathbf{k}}^{\dagger}|0 \rangle|^2 \delta(E_m - E_0 + \omega)) \quad (16)$$

via the independent analytical continuations

$$\begin{aligned} \langle c_{\mathbf{k}}(\tau)c_{\mathbf{k},\alpha}^{\dagger}(0) \rangle &= \int d\omega e^{-\tau\omega} A_+(\omega) \\ \langle c_{\mathbf{k}}^{\dagger}(\tau)c_{\mathbf{k},\alpha}(0) \rangle &= \int d\omega e^{-\tau\omega} A_-(\omega) \end{aligned} \quad (17)$$

with $A(\omega) = A_+(\omega) + A_-(-\omega)$. Here, $|0\rangle$ in Eq. (16) is the ground state at finite doping and $\langle n|$ is an eigenstate of the Hamiltonian with energy E_n and an additional particle (hole) relative to the ground state. In Fig. 11, we plot the spectral functions for $L = 21$ and $\delta = 0, \frac{1}{441}, \frac{3}{441}$ and $\frac{4}{441}$ ($2L^2 - N_p = 0, 2, 6$ and 8). The dominant feature follows the mean-field BCS form $E(\mathbf{k}) = \pm\sqrt{(\epsilon(\mathbf{k}) - \mu)^2 + |\Delta|^2}$, where $\pm\epsilon(k)$ denotes the Dirac dispersion of the honeycomb lattice. This result shows that the Goldstone modes do not strongly couple to single-particle excitations.

In fact, the Green's function at the Γ point has a special property, due to a commutation rule between the fermion operator and the interaction term of Hamiltonian (we use the notation $\mathbf{c}_i^{\dagger} = (\hat{c}_{i,\uparrow}^{\dagger}, \hat{c}_{i,\downarrow}^{\dagger})$)

$$\left[\sum_i \hat{c}_{i,\alpha}, \sum_{\diamond} \left(\sum_{\langle\langle ij \rangle\rangle \in \diamond} iv_{ij} \hat{c}_i^{\dagger} \boldsymbol{\sigma} \hat{c}_j + H.c. \right) \right]^2 = 0. \quad (18)$$

The above relation follows directly from

$$\left[\sum_i \hat{c}_{i,\alpha}, \sum_{\langle\langle ij \rangle\rangle \in \diamond} iv_{ij} \hat{c}_i^{\dagger} \boldsymbol{\sigma} \hat{c}_j + H.c. \right] = 0 \quad (19)$$

which holds for the summation of spin-orbit operators inside each hexagon and for any vector $\boldsymbol{\sigma}$ in the space of Pauli matrices $\sigma_x, \sigma_y, \sigma_z$. Hence, the Green's function $\langle \hat{c}_{\mathbf{k}}^{\dagger}(\tau) \hat{c}_{\mathbf{k}}(0) \rangle$ at the $\mathbf{k} = \Gamma$ point is identical to that of the non-interacting Hamiltonian.

Finite-temperature calculation

In contrast to the projective approach, the finite-temperature auxiliary field QMC (FTQMC) algorithm is formulated in the grand-canonical ensemble. Adding a chemical potential term, $-\mu \sum_i \hat{c}_i^{\dagger} \hat{c}_i$, to the Hamiltonian, see Eq. (1) of the main text, allows us to compute the doping away from half-filling ($\mu = 0$):

$$\delta \equiv \frac{\langle \sum_i \hat{n}_i \rangle}{2L^2} - 1. \quad (20)$$

Figure 12 shows the corresponding result for the case where the inverse temperature β and the system size L scale as $\beta = L^2/3$. This implicitly makes the assumption that $z = 2$. Overall, our limited data are consistent with the more efficient PQMC calculation. At large values of

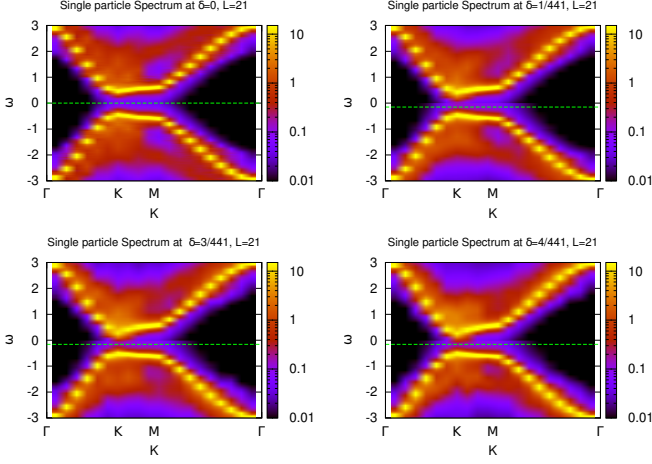


FIG. 11. Single-particle spectrum at dopings (a) $\delta = 0$, (b) $\frac{1}{441}$, (c) $\frac{3}{441}$, and (d) $\frac{4}{441}$. The green dotted line is the chemical potential μ evaluated from Eq. (3) of the main text.

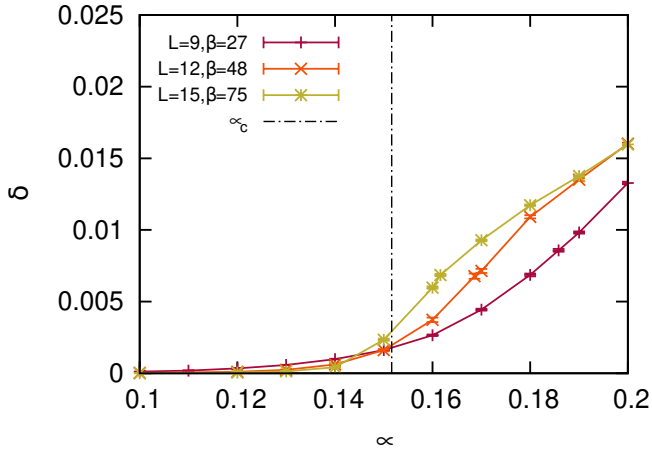


FIG. 12. Doping factor δ as a function of chemical potential μ from FTQMC simulations, with sizes $L = 9, 12$ and 15 , and $\beta = \frac{1}{3}L^2$.

δ , results for $L = 12$ and $L = 15$ are consistent with a linear dependence of δ on μ that overshoots the critical chemical potential and suggest $z > 2$.

From the numerical point of view, the FTQMC is not as efficient as the PQMC. The numerical cost to reach the low-temperature limit scales as $V^3\beta^z$. We have also noticed long warm-up and autocorrelation times to equilibrate the particle number in the vicinity of $\mu = \mu_c$.

Mean-field calculation

In this section, we summarize the details of our mean field calculation. Expanding interacting part of Eq. (1)

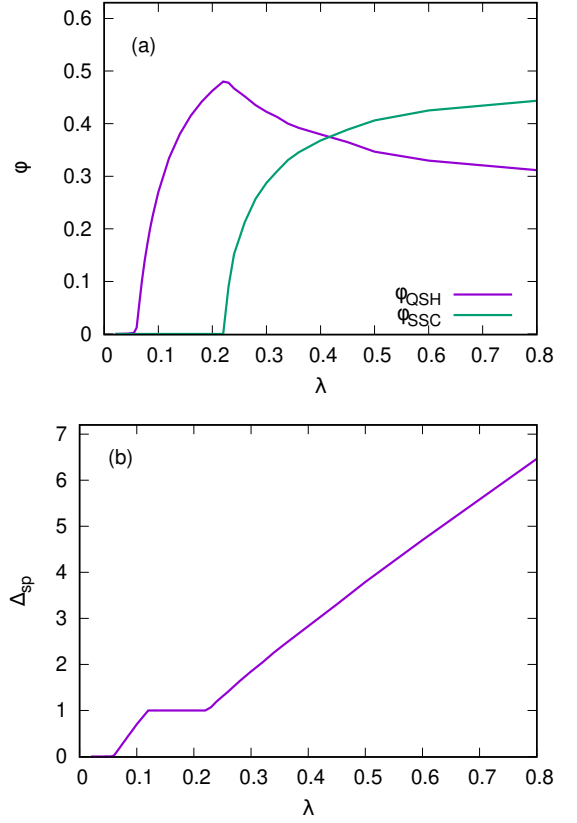


FIG. 13. Mean-field solution as a function of λ at half-filling. (a) QSH and SSC order parameters. (b) Fermionic single-particle gap.

of the main text as

$$\begin{aligned}
 H_V &= -\lambda \sum_{\square} \left(\sum_{\langle\langle ij \rangle\rangle} i\nu_{ij} \hat{c}_i^\dagger \sigma \hat{c}_j + H.c. \right)^2 \\
 &= -\lambda \sum_{\square} \sum_{\langle\langle ij \rangle\rangle} \sum_{\langle\langle i'j' \rangle\rangle \neq \langle\langle ij \rangle\rangle} \hat{\mathbf{J}}_{\langle\langle i,j \rangle\rangle} \cdot \hat{\mathbf{J}}_{\langle\langle i',j' \rangle\rangle} \quad (21) \\
 &\quad - \lambda \sum_{\square} \sum_{\langle\langle ij \rangle\rangle} [+6\hat{\eta}_i^\dagger \hat{\eta}_j + h.c. - 4\hat{\mathbf{S}}_i \cdot \hat{\mathbf{S}}_j \\
 &\quad - 5\hat{n}_i \hat{n}_j + 5(\hat{n}_i + \hat{n}_j)]
 \end{aligned}$$

where

$$\begin{aligned}
 \hat{\mathbf{J}}_{\langle\langle i,j \rangle\rangle} &\equiv i\nu_{ij} \hat{c}_i^\dagger \sigma \hat{c}_j + H.c., \\
 \hat{\eta}_i &\equiv \hat{c}_{i\downarrow} \hat{c}_{i\uparrow}, \quad \hat{\eta}_i^\dagger \equiv \hat{c}_{i\uparrow}^\dagger \hat{c}_{i\downarrow}^\dagger, \quad (22) \\
 \hat{\mathbf{S}}_i &\equiv \frac{1}{2} \hat{c}_i^\dagger \sigma \hat{c}_i.
 \end{aligned}$$

The self-consistent calculation is based on selecting a polarization direction for the three (two) components of the QSH (SSC) order parameter. The calculation is done by numerically minimizing the free energy in the space of

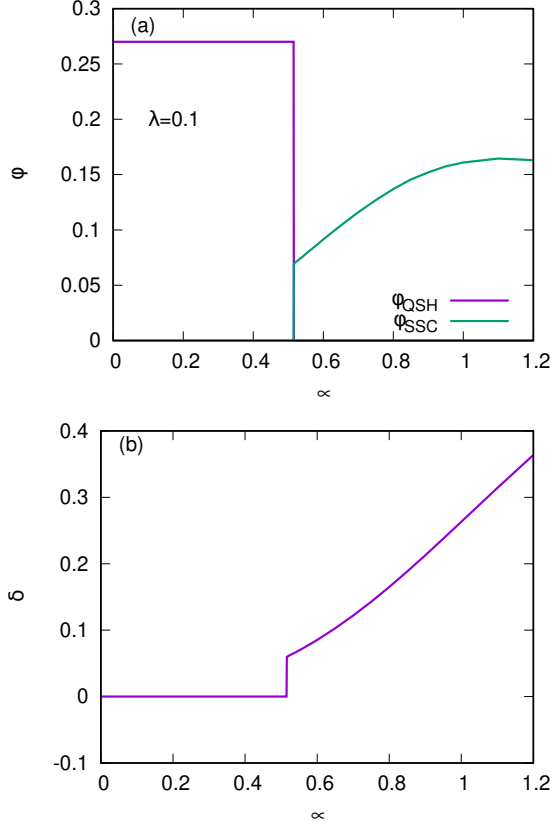


FIG. 14. Mean-field solution as a function of chemical potential μ at $\lambda = 0.1$. (a) QSH and SSC order parameters. (b) Doping factor δ .

the two order parameters

$$f(\beta)_\phi = \frac{-1}{\beta V} \ln \text{Tr} e^{-\beta(H_T + H_V) - 15\beta V \lambda \phi_{\text{QSH}}^2 - 36\beta V \lambda \phi_{\text{SSC}}^2} \quad (23)$$

where

$$\begin{aligned} H_T &= -t \sum_{\langle i,j \rangle} (\hat{c}_i^\dagger \hat{c}_j + H.c.) + \mu \sum_i \hat{c}_i^\dagger \hat{c}_i \\ H_V &= -5\lambda \sum_{\square} \sum_{\langle\langle i,j \rangle\rangle} \phi_{\text{QSH}} \cdot \hat{J}^z_{\langle\langle i,j \rangle\rangle} \\ &\quad - 36\lambda \sum_i \phi_{\text{SSC}} \hat{\eta}_i^x. \end{aligned} \quad (24)$$

We consider a paramagnetic saddle point with $\langle \hat{S}_i \rangle = 0$ and $\langle \hat{n}_i \rangle = 1 - \delta$. Thus, for any local minimum of Eq. (23) with $\frac{\partial f}{\partial \phi_{\text{QSH}}} = 0$ and $\frac{\partial f}{\partial \phi_{\text{SSC}}} = 0$,

$$\begin{aligned} \phi_{\text{QSH}} &= \frac{1}{6} \sum_{\langle\langle i,j \rangle\rangle} \langle \hat{J}^z_{\langle\langle i,j \rangle\rangle} \rangle \\ \phi_{\text{SSC}} &= \frac{1}{2} \langle \hat{\eta}_{i,A}^x + \hat{\eta}_{i,B}^x \rangle \end{aligned} \quad (25)$$

which holds locally due to translational symmetry. We

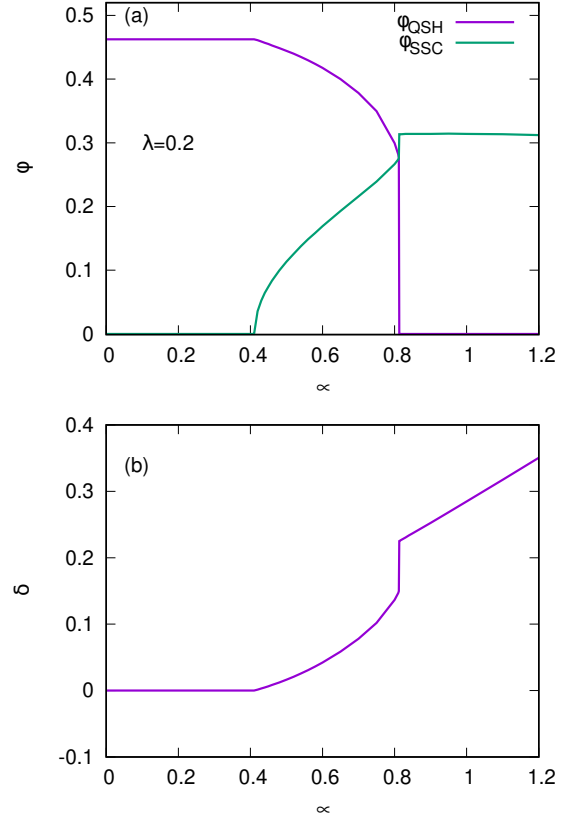


FIG. 15. Mean-field solution as a function of chemical potential μ at $\lambda = 0.2$. (a) QSH and SSC order parameters. (b) Doping factor δ .

numerically integrated over the Brillouin zone of an $L = 120$ lattice and took the zero-temperature limit $\beta \rightarrow \infty$.

The two order parameters as a function of λ in the half-filled case are shown in Fig. 13(a). We observe a semimetal ($\phi_{\text{QSH}} = \phi_{\text{SSC}} = 0$), a pure QSH state ($\phi_{\text{QSH}} \neq 0, \phi_{\text{SSC}} = 0$), a pure SSC state ($\phi_{\text{QSH}} = 0, \phi_{\text{SSC}} \neq 0$), as well as a coexistence (QSH+SSC) state ($\phi_{\text{QSH}} \neq 0, \phi_{\text{SSC}} \neq 0$). Since charge conservation is a protecting symmetry of the QSH insulator, the transition between the QSH and QSH+SSC states can be continuous without a closing of the single-particle gap (see Fig. 13(b)).

On the other hand, upon doping the pure QSH state, the phase diagram exhibits two distinct mean-field scenarios. Two representative examples at $\lambda = 0.1$ and $\lambda = 0.2$ are shown in Figs. 14 and 15, respectively. In the case of $\lambda = 0.1$ (Fig. 14), which is close to the Gross-Neveu transition, a clear first-order transition between the QSH and SSC phases is observed. Doping at $\lambda = 0.2$ (Fig. 15) leads to two phase transitions: (i) a $z = 2$ transition from the pure QSH state to the coexistence state at $\mu \approx 0.4$, characterized by a linear growth of δ and (ii) a first-order phase transition to an SSC state at $\mu \approx 0.8$. Such first-order transitions are characterized by a level crossing corresponding to two local minima in the free-

energy density in Eq. (23).